RSC Advances

PAPER

View Article Online
View Journal | View Issue

Cite this: *RSC Adv.*, 2015, **5**, 4609

Facile synthesis of hollow In_2O_3 microspheres and their gas sensing performances

Xiaolong Hu,[a] Xin Zhou,[a] Biao Wang,[b] Peng Sun,*[a] Xiaowei Li,[a] Chen Wang,[a] Jiangyang Liu[a] and Geyu Lu*[a]

Received 12th October 2014
Accepted 11th December 2014

DOI: 10.1039/c4ra12244e

www.rsc.org/advances

Hollow In_2O_3 microspheres constructed by primary nanoparticles were successfully prepared by thermal treatment of the precursor, which was synthesized *via* a facile chemical solution route without any templates or surfactants. The images of field emission scanning electron microscopy (FESEM) and transmission electron microscopy (TEM) indicated that the sample was composed of a large number of hollow In_2O_3 microspheres with diameters of 1–2 μm. In addition, a gas sensor based on the In_2O_3 hollow microspheres was fabricated and its gas sensing performances were investigated. It was found that sensors based on the as-prepared sample had a low operating temperature (80 °C), and exhibited high response, low detection limit and excellent selectivity to NO_2.

1. Introduction

In the past decade, the investigation of oxide semiconductors for gas sensing applications has become a hot topic because of increasing safety concerns for the environment and industrial activities.[1–3] For oxide semiconductor gas sensors, high sensitivity and excellent selectivity are the two most important parameters. Therefore, developing new strategies to increase sensitivity and improve the selectivity of sensors represent one of the major scientific challenges. A critical element in the pursuit of this quest is the discovery of efficient and cost-effective sensing materials. Due to well-defined interior voids, good surface permeability, low density, and high specific surface area, hollow structural sensing materials have attracted growing interest in recent years.[4–9] Generally, the syntheses depend on complicated templating approaches,[9–11] in which hard or soft sacrificial templates are used to create a hollow structure. However, template contamination mostly decreases the activity of sensing materials and the synthetic procedure is tedious and high cost. In this regard, it is still highly desirable to develop facile, solution-based, and template free self-assembly methods for the preparation of hollow structures.

Indium oxide (In_2O_3) is a very important wide-band-gap (E_g = 3.6 eV) n-type semiconductor, well-known for its useful optoelectronic properties.[12–14] In_2O_3 nanostructures can be synthesized *via* various methods and have found use in a variety of electronics applications.[15–17] They are also of some interest as gas sensors, which have been found to be particularly sensitive to reducing gases[18,19] such as ethanol and oxidizing gases[20,21] such as nitrogen dioxide and ozone. Many studies have been conducted in order to improve the performance of gas sensors by reducing the size of In_2O_3 since Yamazoe demonstrated that a reduction in crystallite size could significantly enhance sensing performance.[22,23] However, the aggregation between the nanoparticles will result in the degradation of the gas sensing properties. Recently, In_2O_3 with hollow structures have been demonstrated to be promising candidates for ultrasensitive sensors due to their unique structures, which are conducive to the diffusion and recognition of gas.[24] Herein, a one-step template-free solvothermal approach is reported for the synthesis of In_2O_3 hollow microspheres. When evaluated as the sensing material for gas sensor, the as-prepared In_2O_3 hollow microspheres manifested high response and excellent selectivity to NO_2 at a relatively low temperature (80 °C).

2. Experimental

2.1 Synthesis of In_2O_3 hollow microspheres

All the reagents in the experiment were purchased from Sinopharm Group Co. Ltd., and directly used without further purification. In a typical synthesis process, 0.26 g of $In(NO_3)_3 \cdot 4.5H_2O$ and 0.5 g of urea were added to 40 mL absolute ethanol under vigorous stirring. After 40 min stirring, the mixture was transferred into a Teflon-lined stainless-steel autoclave and maintained at 160 °C for 12 h. After the autoclave was cooled to room temperature naturally, the precipitates were washed with deionized water and absolute ethanol for several times using centrifuge, and then dried at 80 °C. The obtained product was then calcined at 500 °C for 2 h in an air atmosphere using a muffle furnace.

[a]*State Key Laboratory on Integrated Optoelectronics, College of Electronic Science and Engineering, Jilin University, Changchun, 130012, People's Republic of China. E-mail: spmaster2008@163.com; lugy@jlu.edu.cn; Fax: +86 431 85167808; Tel: +86 431 85167808*

[b]*Changchun Institute of Optics, Fine Mechanics and Physics, Chinese Academy Sciences, Changchun 130033, People's Republic of China*

2.2 Characterization

X-ray diffraction (XRD) patterns were recorded on a Rigaku D/Max-2550V X-ray diffractometer with Cu-Kα radiation (λ = 1.5406 Å) to analyze the crystal phases of the synthesized samples. The morphology of the product was examined by field emission scanning electron microscopy (FESEM, JEOL JSM-7500F microscope operated at an acceleration voltage of 15 kV). Transmission electron microscopic (TEM), high-resolution transmission electron microscopic (HRTEM), and the corresponding selected-area electron diffraction (SAED) measurements were performed on a JEOL JEM-2100F transmission electron microscope with an acceleration voltage of 200 kV.

2.3 Fabrication and measurement of gas sensors

The as-prepared powder was mixed with deionized water to make a paste, which was then coated onto an alumina tube (4 mm in length, 1.2 mm in external diameter, and 0.8 mm in internal diameter, attached with a pair of gold electrodes) by a small brush to form a thick film. The thickness of sensing films was about 100 μm. After drying at room temperature for 30 min, the sensing devices were sintered at 400 °C for 2 h. A Ni–Cr heating wire was used to adjusting the operating temperature of the sensor. Finally, the sensor was constructed by connecting the corresponding junctions to the socket of sensor. A photo of the fabricated sensor was presented in Fig. 1, and the corresponding parts of the sensor were marked in this figure. The measurement was processed by a static process in a test chamber which is made of glass. Environmental air was used as both a reference gas and a diluting gas to obtain desired concentrations of target gases. A given amount of the tested gas was injected into the test chamber, and the sensor was put into the chamber for the measurement of the sensing performance. When the response reached a constant value, the upper cover of the test chamber was removed and the sensor began to recover in air. The response of the sensor was defined as R_g/R_a for oxidizing gas and R_a/R_g for reduction gas, here R_g and R_a were the resistances of the sensor in the target gas and air, respectively. The response and recovery times are defined as the time taken by the sensor to achieve 90% of the total resistance change in the case of adsorption and desorption, respectively.

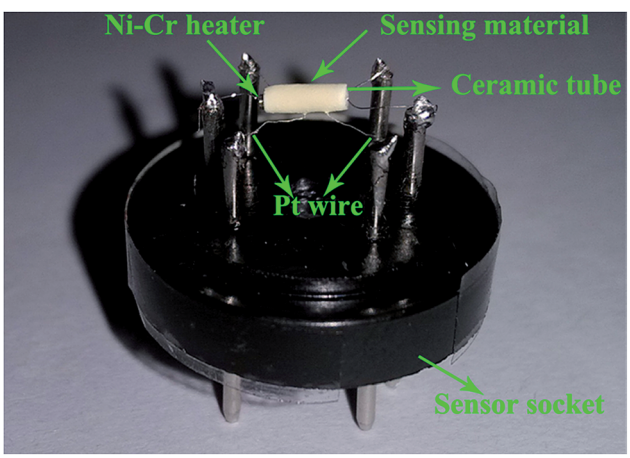

Fig. 1 Photograph of the fabricated sensor.

3. Results and discussion

3.1 Structural and morphological characteristics

The typical XRD pattern of the sample is shown in Fig. 2, from which all the diffraction peaks could be very well indexed to the cubic structure of In_2O_3 with the lattice parameter of $a = 10.118$ Å, which were in good consistent with the standard file JCPDS no. 06-416 and the diffraction peaks in the XRD pattern are of high relative intensity, indicating the high crystallinity and high purity of the samples. The mean crystallite size of In_2O_3 was calculated to be around 16.6 nm using the Debye–Scherrer equation ($D = 0.89\lambda/(\beta \cos \theta)$).

Field emission scanning electron microscopy (FESEM) observations were carried out to get insight into the morphology of In_2O_3 products. Fig. 3 presents a panoramic FESEM image of the In_2O_3 sample, which indicates that it was composed of spherical structures with sizes ranging from 1–2 μm. The hollow interior space can be clearly observed from the enlarged FESEM image of cracked microsphere (the inset of Fig. 3). Furthermore, numerous primary particles with size of tens of nanometres piled up the hollow structure.

Further detailed morphological and structural analysis of the hollow microsphere was carried out using TEM, HRTEM and the corresponding SAED. The hollow nature of the In_2O_3 spheres could be further confirmed in the strong contrast between the dark edge and pale centre in the TEM image of an individual sphere (Fig. 4a), and it can be also observed that nanoparticles constructed the hollow spheres. The corresponding SAED pattern (Fig. 4b) demonstrated that the In_2O_3 hollow microspheres were polycrystalline structures in nature. Fig. 4c exhibits the HRTEM image obtained from the marked fringe of the In_2O_3 nanoparticles in Fig. 4a, from which the lattice fringes could be clearly observed and the distance of the

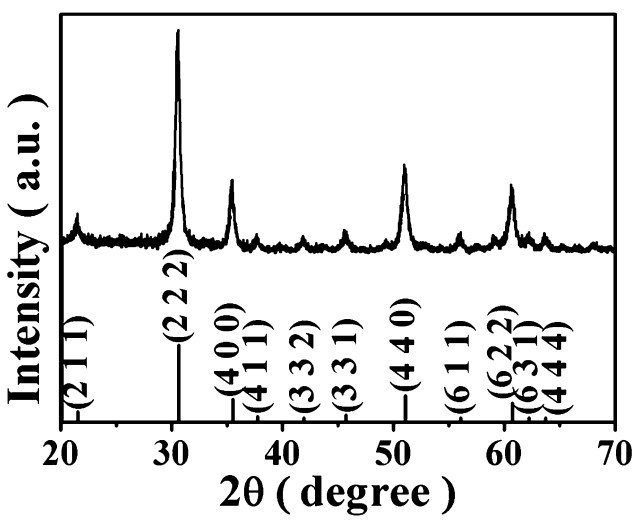

Fig. 2 XRD pattern of the In_2O_3 hollow microspheres and the standard XRD pattern of In_2O_3 (JCPDS no. 06-416).

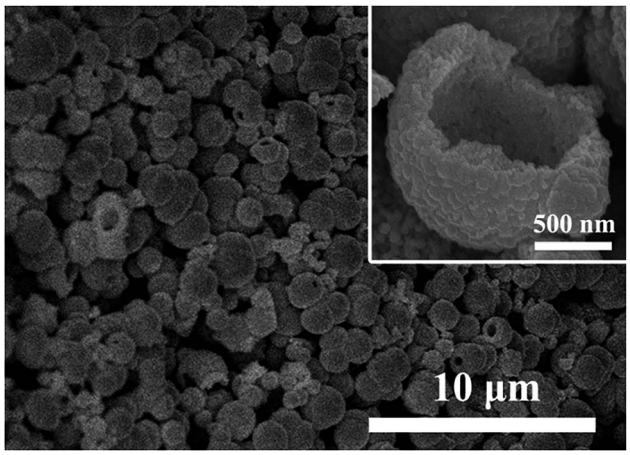

Fig. 3 A panoramic FESEM image of the In_2O_3 sample. The inset shows a cracked microsphere.

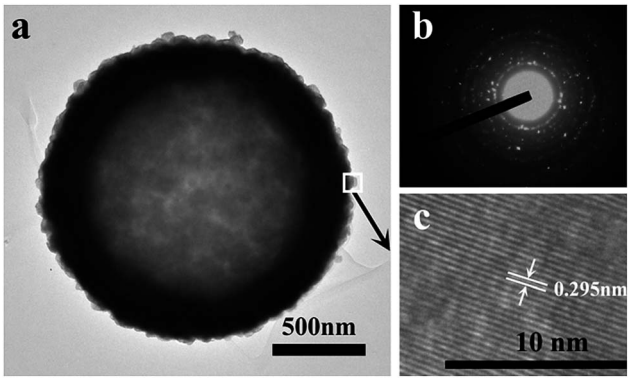

Fig. 4 (a) TEM image, (b) SEAD pattern and (c) HRTEM image of the calcined product (12 h).

adjacent lattice planes was measured to be 0.295 nm, corresponding to the (222) planes of In_2O_3.

To understand the formation process of the hollow In_2O_3 microspheres, a series experiments were carried out at different reaction time (2 h, 8 h, and 12 h), and the evolutions of structure and morphologies of the calcined samples were examined by FESEM. As shown in Fig. 5, the growth process could be clearly divided into three stages. In the first stage (2 h, Fig. 5a), solid spherical structures with very rough surface that composed of nanoparticles and nanosheets could be observed. With increasing reaction time (8 h, Fig. 5b), the surface of the spheres became less rough and the hollow characteristic emerged, which is the typical behaviour of ripening process. Upon prolonging reaction time to 12 h (Fig. 5c), microspheres with hollow internal structure and rough surface were obtained. In general, the formation process could be summarized as a rapid self-assembly of nanosheets and nanoparticles into solid microspheres, followed by the component part that packed at the centre dissolved and transferred to the exterior. Based on the above analysis, Ostwald ripening process could be employed to explain the growth process.[25–27]

3.2 Gas sensing properties

The gas sensing performances of the sensor using hollow In_2O_3 microspheres were investigated. It is well known that the gas-sensing properties of a semiconductor gas sensor are significantly influenced by the operation temperature.[28] Because the adsorption/desorption processes and the competition for chemisorptions between NO_2 and atmospheric oxygen O_2 for the same active surface sites chemisorptions are both regulated by the temperature.[29] To find out the influence of the temperature to the fabricated sensor, the response, response time and recovery time towards 500 ppb NO_2 were tested at varying operation temperature, as shown in Fig. 6. It is obvious that the response to NO_2 increased with the decrease of temperature, and the fabricated sensor exhibited excellent response to NO_2 at relatively low temperature. The response to 500 ppb NO_2 at 120 °C, 100 °C, 80 °C, 60 °C and 40 °C were about 47.5, 193.7, 323.5, 674.1 and 879.9, respectively. So the fabricated sensor could operate at relatively low temperature, which meant low power consumption and this was very important for a gas sensor to be put into use. Apart from response, response time and recovery time also need to be considered to comprehensive measure the gas sensing performance of a gas sensor. The correlation of the response time and recovery time with the operation temperature were presented in the inset of Fig. 6b. As can be seen, the response time and recovery time also increased with the decrease of temperature. Roughly speaking, with the decrease of the temperature, the gas molecules became less and less

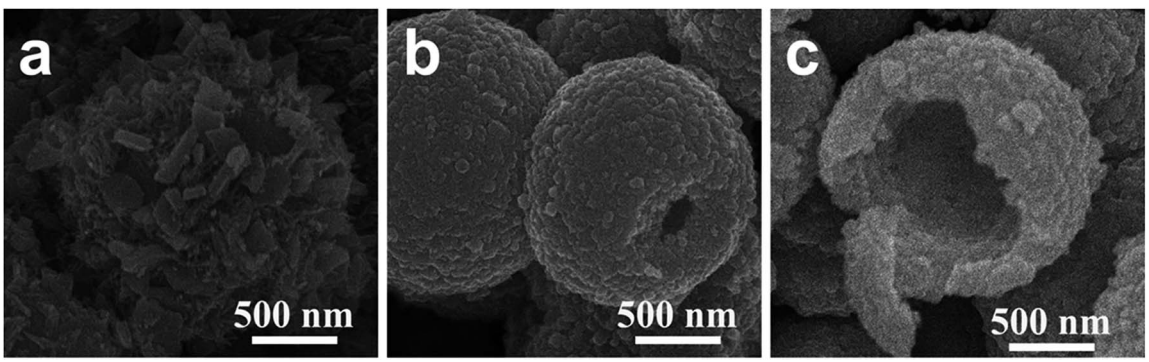

Fig. 5 SEM images of morphology evolution of hollow In_2O_3 microspheres prepared with different reaction time: (a) 2 h, (b) 8 h, (c) 12 h.

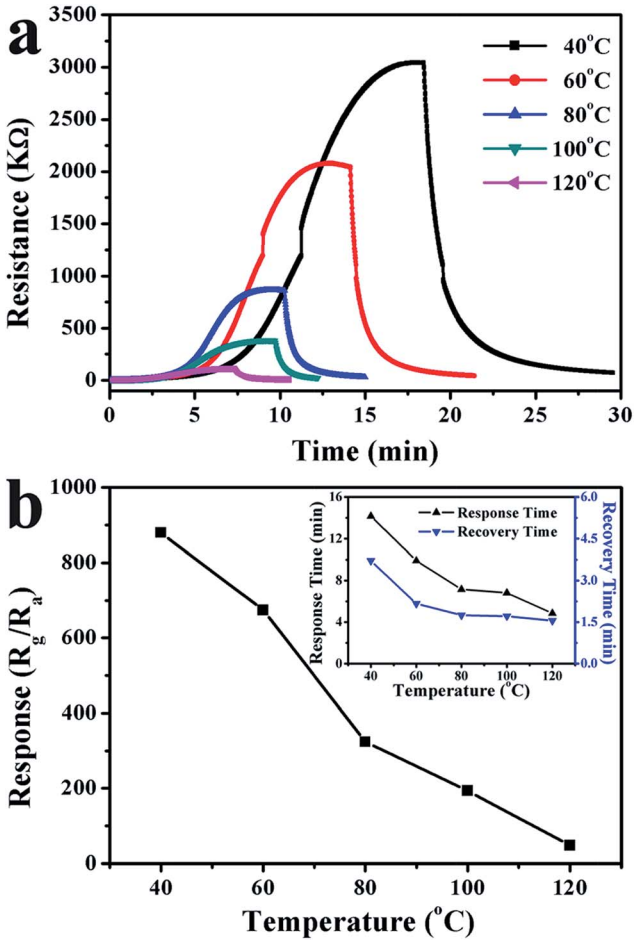

Fig. 6 (a) The dynamic response resistances of the fabricated sensor to 500 ppb NO_2 at 40 °C, 60 °C, 80 °C, 100 °C and 120 °C. (b) The correlation of the response with the operation temperature. And (inset of b) the correlation of the response/recover time with the operation temperature.

active which led to the increase of the response time and recovery time. But the decrease of the temperature would also make the gas adsorption easier and the depth of gas diffusion deeper which will cause the high utilization rate of the sensing material, thus leading to higher response.[30–34] Moreover, when the temperature was higher than 80 °C, the change of temperature had not obvious effects on the response time and recovery time. Therefore, although the response to 500 ppb NO_2 at 80 °C (323.5) was not the highest, considering response time and recovery time, 80 °C was chosen to be the optimal operation temperature of the fabricated sensor for NO_2 detection, which was employed to further investigate the sensing performances.

The relationship between response and NO_2 concentrations for the sensor at the operating temperature of 80 °C is displayed in Fig. 7a. From the curve, it is found that the responses of sensor increased with the gas concentration. The response to 50, 100, 200, 300, 400 and 500 ppb NO_2 were about 2.0, 3.1, 6.1, 39.1, 119.8 and 323.5, respectively. It is worth noting that the sensor showed an obvious response (2.0) even to NO_2 concentration as low as 50 ppb, which indicated that

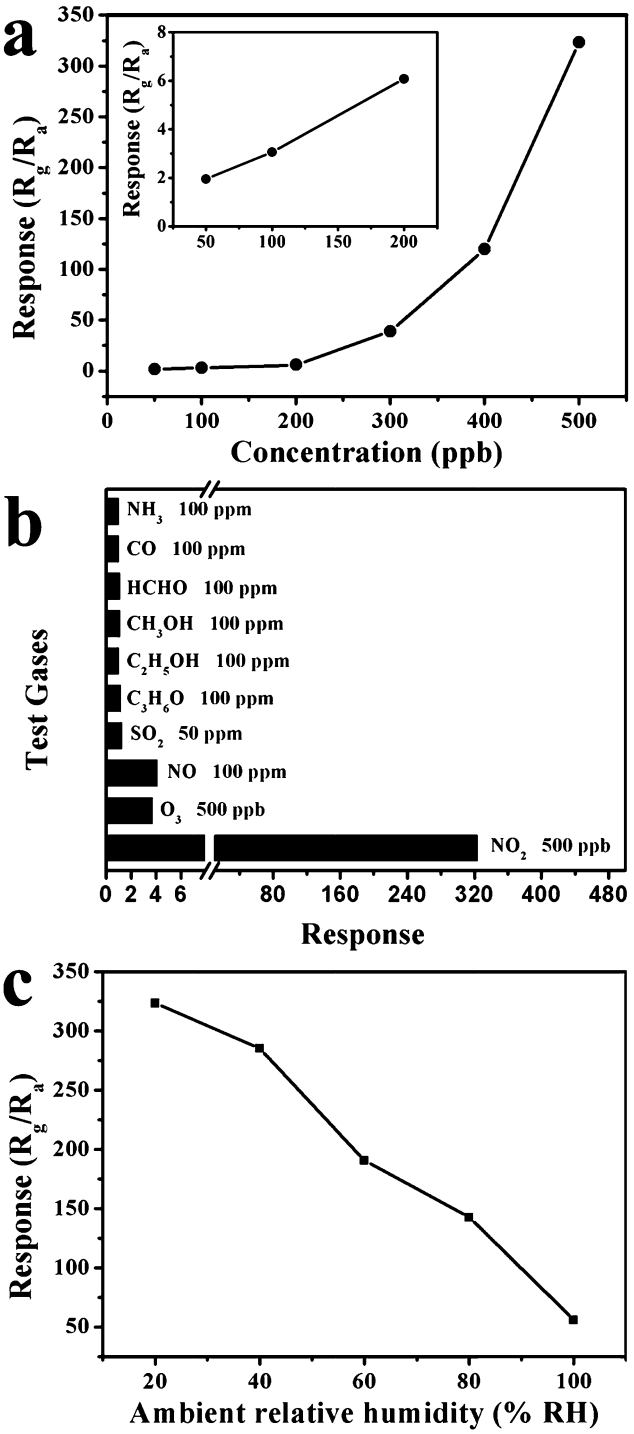

Fig. 7 (a) Response of the sensor *versus* NO_2 concentrations in the range of 50–500 ppb at 80 °C. (b) Response of the sensor to various test gases at 80 °C. (c) Response of the sensor to 500 ppb NO_2 under different relative humidity at 80 °C.

the sensor had a relatively low detection limit (shown in the inset of Fig. 7a). A comparison between the sensing performances of the sensor presented in this paper and literature reports is summarized in Table 1. It is noteworthy that the sensor fabricated in our work exhibits better sensing performance compared with those reported in the literature.

Table 1 Comparison of gas-sensing characteristics of sensing material in present work and those reported in the literatures

Material	NO_2 concentration	Temperature (°C)	Sensor response	Reference
Ordered mesoporous Fe-doped In_2O_3	1 ppm	150	71	43
Mesoporous In_2O_3 (UV light-enhanced)	5 ppm	100	37.8	44
Root slice-like In_2O_3 microspheres	5 ppm	250	1.5	45
Zn–In_2O_3 flower-like structures	5 ppm	300	~27.4	46
WO_3 thin films	10 ppm	150	57	47
WO_3 hollow microspheres	1 ppm	300	~54	48
Hollow In_2O_3 microspheres	500 ppb	80	737.8	Present work

Except for response, response time and recovery time, selectivity is also an important parameter for gas sensor. Eight kinds of other gases were tested, including 100 ppm NO, NH_3, CO, methanol, methanol, ethanol and acetone, 50 ppm SO_2, and 500 ppb O_3. The test results are presented in Fig. 7b. It is clear that the fabricated sensor exhibits the highest response to NO_2 among all these tested gases, and the response to 500 ppb NO_2 was at least dozens of times higher than the other tested gases at the optimum operation temperature (80 °C). The test results indicated that the gas sensor based on the hollow microspheres In_2O_3 possess an excellent selectivity to NO_2 against the other test gases.

The responses of the fabricated sensor to 500 ppb NO_2 under different relative humidity at 80 °C were also tested to find out the effect of the humidity on the response of the sensor. And the results were presented in Fig. 7c. The results indicated that the response decreased with the rise of relative humidity almost linearly. According to D. Vlachos *et al.*,[35] the decrease might be caused by the active sites on the material surface were covered gradually by water molecules.

The most widely accept sensing mechanism of the sensor based on In_2O_3 to NO_2 gas can be stated as follow.[36–42] The electrical conductivity of In_2O_3 derives from electron transfer between In^{2+} and In^{3+}, the formation of the In^{2+} occurring through oxygen deficiency (eqn (1)). Anion vacancies $V_O^{\cdot}$ and mainly partially reduced cations In^{2+} are the surface basic sites $(S_b)_s$ for NO_2 chemisorption. And the formation of the chemisorption bond continued on the charge transfer from active sites $(S_b)_s$ into an orbital of NO_2 causes a reduction in the strength of N–O bonds that makes the decomposition of the NO_2 molecules easier. Therefore, NO_2 molecules were reduced into NO or N_2 and the electronics of the In_2O_3 sensing materials were captured which led to the increase of the resistance of the sensor. The sensing mechanism could be summarized according to the following equations.

$$In_2O_3 \rightarrow In_{2-x}{}^{3+}In_x{}^{2+}O_{3-x}V_{O\times}^{\cdot} + \frac{1}{2}O_2 \quad (1)$$

$$NO_{2,gas} + In^{2+} \rightarrow (In^{2+} - NO_{2,ads}) \rightarrow (In^{3+} - O_{ads}{}^{-}) + NO_{gas} \quad (2)$$

$$NO_{gas} + In^{2+} \rightarrow (In^{2+} - NO_{ads}) \rightarrow (In^{3+} - O_{ads}{}^{-}) + \frac{1}{2}N_2 \quad (3)$$

$$NO_{2,\,gas} + V_O^{\cdot} \rightarrow \left(V_O - NO_{2,\,ads}{}^{-}\right) \rightarrow \left(V_O - O_{ads}{}^{-}\right) + NO_{gas} \quad (4)$$

$$NO_{gas} + V_O^{\cdot} \rightarrow (V_O - NO_{ads}{}^{-}) \rightarrow (V_O - O_{ads}{}^{-}) + \frac{1}{2}N_2 \quad (5)$$

4. Conclusions

In summary, hollow In_2O_3 microspheres had been successfully synthesized by a simple solvothermal method and subsequent annealing process. FESEM and TEM images displayed that the microspheres were composed of nano-sized primary particles. Moreover, gas sensors based on the as-obtained hollow microspheres were fabricated and their sensing performances were investigated. It was found that the sensor exhibited high response, low detection limit and excellent selectivity to NO_2 at a low operating temperature (80 °C).

Acknowledgements

This work is supported by the National Nature Science Foundation of China (no. 61374218, 61134010, and 61327804) and Program for Chang Jiang Scholars and Innovative Research Team in University (no. IRT13018). National High-Tech Research and Development Program of China (863 Program, no. 2013AA030902 and 2014AA06A505).

Notes and references

1 A. Jerger, H. Kohler, F. Becker, H. B. Keller and R. Seifert, *Sens. Actuators, B*, 2002, **81**, 301–307.
2 S. Ampuero and J. O. Bosset, *Sens. Actuators, B*, 2003, **94**, 1–12.
3 N. Barsan, D. Koziej and U. Weimar, *Sens. Actuators, B*, 2007, **121**, 18–35.
4 X. Zhou, C. Wang, W. Feng, P. Sun, X. Li and G. Lu, *Mater. Lett.*, 2014, **120**, 5–8.
5 Y. Cai, X. Li, Y. Liu, S. Du, P. Cheng, F. Liu, K. Shimanoe, N. Yamazoe and G. Lu, *CrystEngComm*, 2014, **16**, 6135–6140.
6 X. Li, W. Feng, Y. Xiao, P. Sun, X. Hu, K. Shimanoe, G. Lu and N. Yamazoe, *RSC Adv.*, 2014, **4**, 28005–28010.
7 P. Sun, X. Zhou, C. Wang, K. Shimanoe, G. Lu and N. Yamazoe, *J. Mater. Chem. A*, 2014, **2**, 1302–1308.

8 C. R. Michel, A. H. Martinez-Preciado, R. Parra, C. M. Aldao and M. A. Ponce, *Sens. Actuators, B*, 2014, **202**, 1220–1228.
9 D. Han, P. Song, H. Zhang, Z. Yang and Q. Wang, *Mater. Lett.*, 2014, **124**, 93–96.
10 S.-J. Kim, I.-S. Hwang, C. W. Na, I.-D. Kim, Y. C. Kang and J.-H. Lee, *J. Mater. Chem.*, 2011, **21**, 18560–18567.
11 Y. Fan, S. Wang and Z. Sun, *Mater. Chem. Phys.*, 2012, **134**, 93–97.
12 R. A. Ismail, O. A. Abdulrazaq and K. Z. Yahya, *Surf. Rev. Lett.*, 2005, **12**, 515–518.
13 Y. Li, W. Cai, G. Duan, F. Sun, B. Cao, F. Lu, Q. Fang and I. W. Boyd, *Appl. Phys. A: Mater. Sci. Process.*, 2005, **81**, 269–273.
14 A. M. E. Raj, K. C. Lalithambika, V. S. Vidhya, G. Rajagopal, A. Thayumanavan, M. Jayachandran and C. Sanjeeviraja, *Phys. B*, 2008, **403**, 544–554.
15 D. E. Williams, *Sens. Actuators, B*, 1999, **57**, 1–16.
16 B. Yaglioglu, H. Y. Yeom, R. Beresford and D. C. Paine, *Appl. Phys. Lett.*, 2006, **89**, 062103.
17 D. H. Zhang, C. Li, S. Han, X. L. Liu, T. Tang, W. Jin and C. W. Zhou, *Appl. Phys. Lett.*, 2003, **82**, 112–114.
18 N. Du, H. Zhang, B. Chen, X. Ma, Z. Liu, J. Wu and D. Yang, *Adv. Mater.*, 2007, **19**, 1641–1645.
19 P. Song, D. Han, H. Zhang, J. Li, Z. Yang and Q. Wang, *Sens. Actuators, B*, 2014, **196**, 434–439.
20 G. Korotcenkov, A. Cerneavschi, V. Brinzari, A. Vasiliev, M. Ivanov, A. Cornet, J. Morante, A. Cabot and J. Arbiol, *Sens. Actuators, B*, 2004, **99**, 297–303.
21 X. Xu, D. Wang, J. Liu, P. Sun, Y. Guan, H. Zhang, Y. Sun, F. Liu, X. Liang, Y. Gao and G. Lu, *Sens. Actuators, B*, 2013, **185**, 32–38.
22 C. Xu, J. Tamaki, N. Miura and N. Yamazoe, *Sens. Actuators, B*, 1991, **3**, 147–155.
23 N. Yamazoe, *Sens. Actuators, B*, 1991, **5**, 7–19.
24 J.-H. Lee, *Sens. Actuators, B*, 2009, **140**, 319–336.
25 X. Li, P. Sun, T. Yang, J. Zhao, Z. Wang, W. Wang, Y. Liu, G. Lu and Y. Du, *CrystEngComm*, 2013, **15**, 2949–2955.
26 Y. Qin, F. Zhang, Y. Chen, Y. Zhou, J. Li, A. Zhu, Y. Luo, Y. Tian and J. Yang, *J. Phys. Chem. C*, 2012, **116**, 11994–12000.
27 X. Chen, X. Jing, J. Wang, J. Liu, D. Song and L. Liu, *CrystEngComm*, 2013, **15**, 7243–7249.
28 V. R. Shinde, T. P. Gujar and C. D. Lokhande, *Sens. Actuators, B*, 2007, **123**, 701–706.
29 X. Xu, P. Zhao, D. Wang, P. Sun, L. You, Y. Sun, X. Liang, F. Liu, H. Chen and G. Lu, *Sens. Actuators, B*, 2013, **176**, 405–412.
30 N. Yamazoe, G. Sakai and K. Shimanoe, *Catal. Surv. Asia*, 2003, **7**, 63–75.
31 A.-M. Andringa, N. Vlietstra, E. C. Smits, M.-J. Spijkman, H. L. Gomes, J. H. Klootwijk, P. W. Blom and D. M. De Leeuw, *Sens. Actuators, B*, 2012, **171**, 1172–1179.
32 N. Yamazoe and K. Shimanoe, *Sens. Actuators, B*, 2008, **128**, 566–573.
33 N. Matsunaga, G. Sakai, K. Shimanoe and N. Yamazoe, *Sens. Actuators, B*, 2003, **96**, 226–233.
34 G. Sakai, N. Matsunaga, K. Shimanoe and N. Yamazoe, *Sens. Actuators, B*, 2001, **80**, 125–131.
35 D. Vlachos, P. Skafidas and J. Avaritsiotis, *Sens. Actuators, B*, 1995, **25**, 491–494.
36 C. S. Rout, K. Ganesh, A. Govindaraj and C. N. R. Rao, *Appl. Phys. A: Mater. Sci. Process.*, 2006, **85**, 241–246.
37 L. Francioso, A. Forleo, S. Capone, M. Epifani, A. M. Taurino and P. Siciliano, *Sens. Actuators, B*, 2006, **114**, 646–655.
38 M. Ivanovskaya, P. Bogdanov, G. Faglia and G. Sberveglieri, *Sens. Actuators, B*, 2000, **68**, 344–350.
39 M. Ivanovskaya, A. Gurlo and P. Bogdanov, *Sens. Actuators, B*, 2001, **77**, 264–267.
40 M. Epifani, J. D. Prades, E. Comini, E. Pellicer, M. Avella, P. Siciliano, G. Faglia, A. Cirera, R. Scotti and F. Morazzoni, *J. Phys. Chem. C*, 2008, **112**, 19540–19546.
41 A. E. Solovjeva, V. A. Zhdanov, V. A. Markov and R. R. Shvangeradze, *Inorg. Mater.*, 1982, **18**, 825–828.
42 A. Gurlo, N. Barsan, M. Ivanovskaya, U. Weimar and W. Gopel, *Sens. Actuators, B*, 1998, **47**, 92–99.
43 J. Zhao, T. Yang, Y. Liu, Z. Wang, X. Li, Y. Sun, Y. Du, Y. Li and G. Lu, *Sens. Actuators, B*, 2014, **191**, 806–812.
44 T. Wagner, C.-D. Kohl, C. Malagu, N. Donato, M. Latino, G. Neri and M. Tiemann, *Sens. Actuators, B*, 2013, **187**, 488–494.
45 Z. Cheng, L. Song, X. Ren, Q. Zheng and J. Xu, *Sens. Actuators, B*, 2013, **176**, 258–263.
46 P. Li, H. Fan, Y. Cai and M. Xu, *CrystEngComm*, 2014, **16**, 2715–2722.
47 Z. Liu, T. Yamazaki, Y. Shen, T. Kikuta and N. Nakatani, *Sens. Actuators, B*, 2007, **128**, 173–178.
48 C.-Y. Lee, S.-J. Kim, I.-S. Hwang and J.-H. Lee, *Sens. Actuators, B*, 2009, **142**, 236–242.

